Estimation of potential denitrification and its spatiotemporal dynamics in seasonally inundated geomorphic units of a large tropical river using satellite data

Gani, Md Ataul; van Dam, Anne A.; van der Kwast, Johannes; McClain, Michael E.; Irvine, Kenneth A.; Gettel, Gretchen M.

DOI
10.1016/j.scitotenv.2024.178287

Publication date
2025

Document Version
Final published version

Published in
Science of the Total Environment

Science of the Total Environment 959 (2025) 178287

Contents lists available at ScienceDirect

Science of the Total Environment

journal homepage: www.elsevier.com/locate/scitotenv

Estimation of potential denitrification and its spatiotemporal dynamics in seasonally inundated geomorphic units of a large tropical river using satellite data

Md Ataul Gani [a,c,d,*], Anne A. van Dam [a], Johannes van der Kwast [b], Michael E. McClain [a,e], Kenneth A. Irvine [a,c], Gretchen M. Gettel [a,f]

[a] Department of Water Resources and Ecosystems, IHE Delft Institute for Water Education, P.O. Box 3015, 2601 DA Delft, the Netherlands
[b] Department of Land and Water Management, IHE Delft Institute for Water Education, P.O. Box 3015, 2601 DA Delft, the Netherlands
[c] Aquatic Ecology and Water Quality Management Group, P.O. Box 47, 6700 AA Wageningen, the Netherlands
[d] Department of Botany, Jagannath University, 1100 Dhaka, Bangladesh
[e] Department of Water Management, Delft University of Technology, P.O. Box 5048, 2600 GA Delft, the Netherlands
[f] Department of Ecoscience, Freshwater Ecology, University of Aarhus, Aarhus, Denmark

HIGHLIGHTS

- Denitrification is mainly influenced by river discharge and geomorphic units (GUs).
- The surface area and number of GUs are the factors that can control denitrification.
- The linear mixed models estimate denitrification across LULC types using Sentinel-2.
- The modelling is effective for showing the spatiotemporal dynamics of denitrification.
- The model is handy in floodplain or lowland areas where inundation is frequent.

GRAPHICAL ABSTRACT

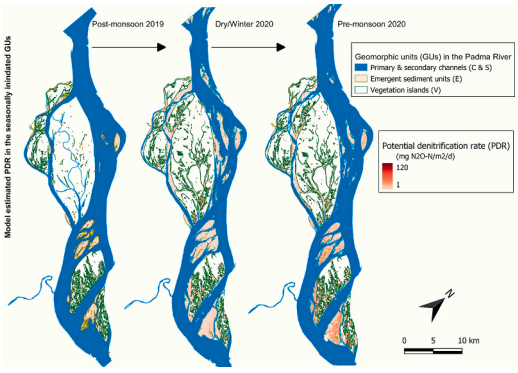

ARTICLE INFO

Editor: Christian Herrera

Keywords:
Sentinel-2
NDVI
Soil moisture
LULC
Linear mixed models (LMMs)

ABSTRACT

Denitrification in large tropical river systems is likely important for nitrogen retention estimates, but is limited by the need for measurements and the ability to scale these estimates to relate seasonal changes to river geomorphology and discharge. Geomorphic units (GUs), that describe the structure of a river system based on their inundation frequency and vegetation cover, may be useful to characterise features that influence denitrification rates. In this study, we tested the hypothesis that measurements of potential denitrification rate (PDR) using denitrification enzyme assays from different GUs could be used to1) relate PDR to soil, vegetation and different land use and land-cover (LULC) types as controlling factors and 2) that these characteristics could be assessed

* Corresponding author at: Department of Water Resources and Ecosystems, IHE Delft Institute for Water Education, P.O. Box 3015, 2601 DA Delft, the Netherlands.
E-mail addresses: ataul.gani@wur.nl, gmdataul@bot.jnu.ac.bd (M.A. Gani), a.vandam@un-ihe.org (A.A. van Dam), h.vanderkwast@un-ihe.org (J. van der Kwast), m.mcclain@un-ihe.org (M.E. McClain), k.irvine@un-ihe.org (K.A. Irvine), g.gettel@ecos.au.dk (G.M. Gettel).

https://doi.org/10.1016/j.scitotenv.2024.178287
Received 3 August 2024; Received in revised form 15 December 2024; Accepted 23 December 2024
Available online 4 January 2025

Padma River
Bangladesh

using remote sensing data to model PDR over a large spatial scale (along a 50 km reach) for the Padma River (Bangladesh). Specifically, 245 PDR measurements were made from the four LULC types with in eight GUs during the dry/winter season 2020. Linear regression using a mixed-modelling approach showed that PDR was highly related to vegetation cover and soil moisture across all GUs. Sentinel-2 data were then used to develop relationships between the Normalised Difference Vegetation Index.

(NDVI) and vegetation cover and, specifically, between Sentinel-2 band 11 and soil moisture, which also reasonably described PDR rates. We then used this satellite data to estimate reach-scale PDR in post-monsoon, dry/winter and pre-monsoon seasons. The satellite-based model showed that PDR increased in GUs from post-monsoon 2019 to pre-monsoon 2020. The vegetation islands and the bars were the most important GUs for denitrification in all seasons. The satellite-assisted approach developed in this study can be applied to the GUs in large lowland rivers where inundation occurs frequently.

1. Introduction

Large rivers are geomorphologically diverse and dynamic, with variations in flow that influence nutrients transport to coastal areas. Water and sediment transport rates alter these systems continuously, creating a variety of recognisable geomorphic units (GUs) (Gupta, 2007; Syvitski et al., 2014), which are considered as building blocks of river morphology (Rinaldi et al., 2015). Seasonally inundated GUs of a lowland river can act like floodplains or riparian zones, making them either sinks or sources for nutrients (Alexander et al., 2000, Tank et al., 2008, Strauss et al., 2011, Ritz et al., 2018;). These potential nutrient retention/export areas can be mapped based on seasonal changes in area exposed (Gani et al., 2022). Among nutrients, nitrogen is of special importance for regulating river productivity (Nanus et al., 2008), but excess nitrogen may cause adverse effects downstream like coastal eutrophication and hypoxia (van Wijk et al., 2022; Ritz and Fischer, 2019; Lin et al., 2020), or contributing to poor river health. Nitrogen in river systems can be conserved through retention, reducing export to the downstream part of the river.

Denitrification is one of the main biogeochemical processes that result in nitrogen loss from natural ecosystems, as nitrate is converted to N_2O and N_2 gases (Davidson and Seitzinger, 2006; Beaulieu et al., 2011; Yao et al., 2016). In rivers, denitrification varies with geomorphology, water residence time, nutrient content and biotic factors (Piña-Ochoa and Álvarez-Cobelas, 2006; Seitzinger et al., 2006; Solomon et al., 2009; Xiong et al., 2017; Korol et al., 2019), particularly oxygen availability

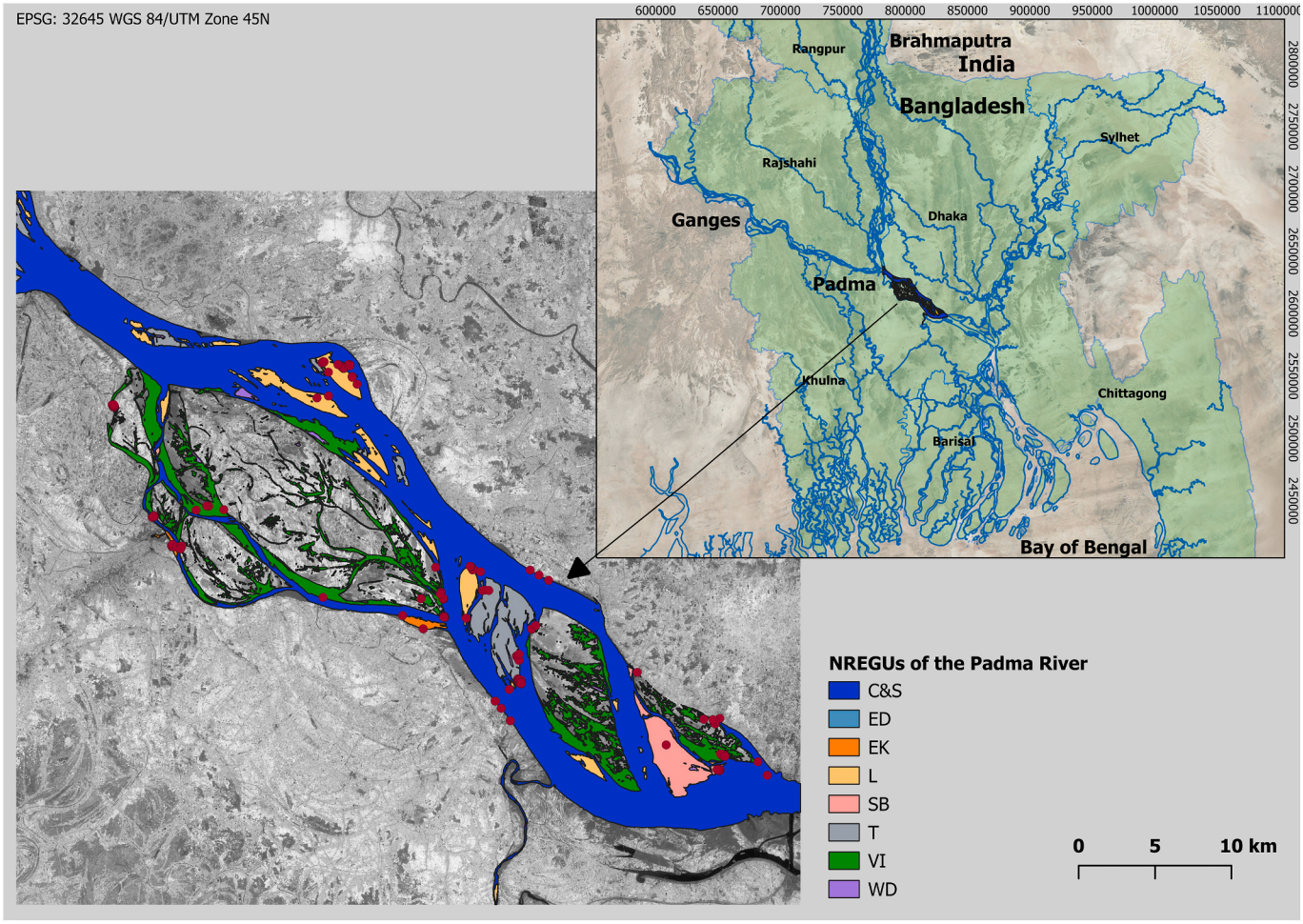

Fig. 1. Study area of Padma River, Bangladesh, showing the classified nutrient retention or export relevant geomorphic units (NREGUs) (C&S=Primary and secondary channels, ED=Dry channel, EK = Unvegetated bank, L = Longitudinal bar, SB = Side bar, T = Transverse bar, VI = Vegetation Island, WD = Water Depression). The red dots in the GUs indicate sampling points.

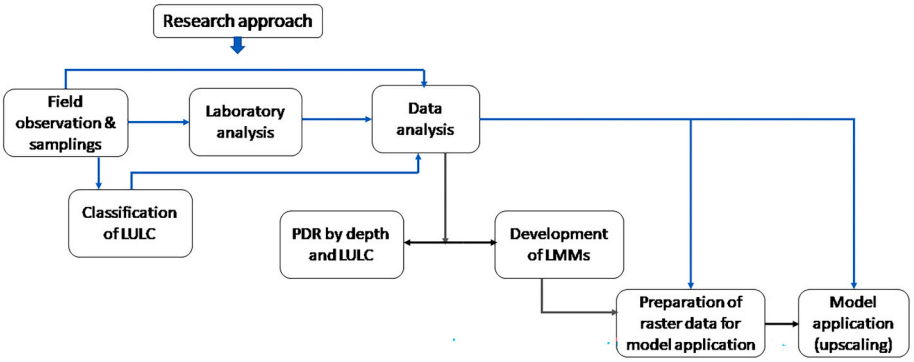

Fig. 2. Overall approach to meet the research objectives.

and concentrations of nitrate and organic carbon (Boyer et al., 2006; Liu et al., 2016; Shrestha et al., 2012; Groffman et al., 1991; Sgouridis and Ullah, 2014). The soil/sediment's water content influences the rate of denitrification (Ding et al., 2019; Garnier et al., 2010; Ullah and Faulkner, 2006; Bai et al., 2005). A high moisture percentage restricts oxygen diffusion, creating favourable conditions for denitrification. Microorganism communities interact in the plant rhizosphere, so the presence or absence of vegetation drives the changes in land use and land cover (LULC), which influence the nitrogen budget in the sediment and, thus, the denitrification process (Audet et al., 2021; Nilsson et al., 2020). Seasonally inundated areas of GUs are characterized by soil/sediment moisture regimes, sediment characteristics, and vegetation dynamics that are important for denitrification.

The spatial variation of LULC types, representing different conditions of oxygen, nitrate and carbon can be used as indirect predictors of denitrification (Kreiling et al., 2019; Xiong et al., 2015; Han et al., 2017). On a larger scale, LULC can be used as a proxy of vegetation dynamics (Guo et al., 2020) and soil moisture (Zucco et al., 2014; Yang et al., 2017). Recent research has shown that temporal variation of inundation should be considered to upscale potential denitrification because this controls nutrient and water supply to the floodplain ecosystems (Kaden et al., 2021). Therefore, many characteristics of the river channel can control denitrification directly or indirectly, but methodological constraints make it difficult to link the spatial dynamics of the river channels to estimates of denitrification.

A number of techniques are available to estimate denitrification rates in soils/sediments (Tuttle et al., 2014; Tatariw et al., 2013; Opdyke et al., 2006). The acetylene inhibition method (Sørensen, 1978) is mostly used because it is relatively simple to apply and allows for analysing large numbers of samples in space and time (Hansen et al., 2016; Groffman et al., 2006). Other methods such as mass balance approaches (Seitzinger et al., 2002), isotope analyses (Sebilo et al., 2017; Böhlke et al., 2004), membrane inlet mass spectrometry (Laursen and Seitzinger, 2002; Pribyl et al., 2005) and modelling (Sun et al., 2017; Hoang et al., 2017; Maavara et al., 2019) have been used based on the conditions of the study sites. For these, however, it is difficult to determine the spatial variability of denitrification across river reaches because of their applicability, complexity and data demand to scale up at the desired level. It is even more complicated when the study area comprises different geomorphic units and is subject to seasonal flood dynamics and LULC changes.

Data derived from remote sensing creates opportunities to quantify biogeochemical processes like denitrification over larger areas; thus, satellite data are used as input data together with process-based measurements. Such an approach was applied in the Amazonian basin to quantify denitrification rates using available carbon and nitrate from in situ data and surface water extent from satellite data (Guilhen et al., 2020). Other researchers suggested that soil moisture might be one of the most relevant factors for scaling up denitrification at an appropriate spatial scale (Martínez-Espinosa et al., 2022, 2021; Robertson et al., 1993).

The Normalised Difference Vegetation Index (NDVI) is a widely used biogeophysical index to estimate vegetation cover (Yi et al., 2022; Dai et al., 2022; Yuan et al., 2013). NDVI is sensitive to inundation, varying according to water depth (Cho et al., 2008; Szabó et al., 2020). Different satellite products are available to estimate soil moisture that can be implemented from very local to large scales (Peng et al., 2021). Sentinel-2 band 11 is a shortwave infrared (1610 nm) (SWIR) band which can be used to discriminate moisture content in soil and vegetation (Holzman et al., 2021). One of the advantages of using Sentinel-2 products is that it can provide high spatial resolution data, i.e. 10 m for its visible and near-infrared bands (VNIR) and 20 m for band 11.

The present study aimed to assess the spatiotemporal distribution of PDR and develop a predictive model based on field-based and satellite data. The specific objectives of the research are to (i) show the influence of LULC in field-based PDR measurement; (ii) determine whether satellite products can be related to soil moisture, vegetation cover, and LULC to model PDR at the reach scale; (iii) use the best model to predict reach-scale estimates of denitrification in the GU's and compare with seasons; and iv) show the impact of GUs on reach-scale denitrification.

2. Material and methods

2.1. Study design and site description

The study area is a roughly50 km reach of the Padma River below the confluence of the Brahmaputra and Ganges rivers (Fig. 1). Seasonal inundation and the erosion and deposition of sediment in the study reach lead to the formation of seasonally inundated GUs, which are classified as primary and secondary channels (C&S), longitudinal bars (L), transverse bars (T), side bars (SB), unvegetated banks (EK), dry channels (ED), vegetated islands (VI) and water depressions (WD) (Gani et al., 2022). Each of these GUs is composed of patches of LULC types that change in area and vegetation cover through the year. During the field observation, five types of LULC were identified and included cropland (CL), natural vegetation (NV), land with water (LW), dry, bare land (DBL) and water bodies (WB). Water depressions (WD) in bars and islands, river edges and any wet portions of the terrestrial GUs were considered in the LW category. In some of the LW land cover types, algal mats were observed. Variations in the area of emergent GUs occur over four seasons. March–May is considered pre-monsoon, June–September is monsoon, October–November is considered post-monsoon, and December to February is considered dry/winter (Gani et al., 2022). The seasonally emergent GUs identified in this study are fully inundated during the monsoon. In the present research, field samples and analyses of denitrification rates were done for GUs in post-monsoon 2019, dry/winter 2020 and pre-monsoon 2020.

2.2. Overall approach

To meet the research objectives, we performed field observation and samplings, laboratory analysis, classification of LULC, and data analysis sequentially, as shown in Fig. 2.

In data analysis, the estimation of PDR by depth and LULC, and the development of linear mixed models (LMMs) were done separately. After developing the LMMs, raster data were prepared for model application, and finally, the model was applied in the GUs to determine spatiotemporal dynamics of PDR (Fig. 2).

2.2.1. Field observation and samplings

During the field visit, spot identification of LULC types in different GUs (identified using Sentinel-2 data) was done, and coordinates were recorded using the Input app (https://inputapp.io, accessed on 25 January 2022) in a smartphone. This app was linked with a geodata repository (Mergin cloud service, https://public.cloudmergin.com, accessed on 25 January 2022) and synchronised within QGIS. In QGIS, the sample points were buffered at a 10-meter distance to convert sampling points into polygons because homogeneous LULCs were found for at least 10 m distances during field observations.

Field sampling was carried out during the dry/low flow season (February 2020). Coordinates and % vegetation cover were estimated at each sampling point within the GUs and recorded to reassess vegetation, if necessary. Simultaneous sediment samples were collected from the sampling points, covering all types of LULC (Fig. 2). Two sets of samples were taken from the top 5 cm (2 times 190 samples) and 5–10 cm (2 times 55 samples) of soil with a 10 cm-diameter PVC ring. All samples were kept separately in Ziplock bags stored in an icebox for the one-two days duration of the field campaign and then transported to the research laboratory in the Department of Botany, Jagannath University, Dhaka, Bangladesh.

2.2.2. Laboratory analysis

In the laboratory, the samples were divided so that one set was used to estimate soil moisture and bulk density and the other denitrification. Samples were processed within 24 h after reaching the laboratory. PDR was estimated by denitrification enzyme activity (DEA) as a part of the acetylene block method as the accumulation of N_2O in the presence of acetylene (Groffman et al., 1999). In the laboratory, sediment samples were placed in gas-tight flasks with a septum port with the addition of media composed of NO_3^- (100 mg N kg^{-1}), dextrose (40 mg kg^{-1}) and chloramphenicol (10 mg kg^{-1}). Anaerobic conditions were established by evacuating and flushing the headspace of flasks with nitrogen three times for 30 s. Then, purified acetylene (98 to 99.5 %) was added, and flasks were placed on a rotary shaker at 125 rpm for half an hour. Gas accumulated in the flask was extracted using a syringe and then injected into evacuated gas vials (15 mL) at three times every 30 min. After processing, the resulting gas vials were transported to IHE Delft Institute for Water Education, the Netherlands. In Delft, N_2O was measured by gas chromatography (Scion 456-GC) using ambient air and standard N_2O concentration with the electron capture detector (ECD) at 250 °C (Groffman et al., 1999).

2.2.2.1. Potential denitrification rate (PDR). Potential denitrification rate (PDR) was calculated as the slope of N_2O produced in the jars over the incubation time. The solubility of N_2O was accounted for using the Bunsen coefficient at 0 °C. Mass-specific denitrification rates were converted to areal rates by using the bulk density. Specifically, PDR was calculated according to the following equations:

$$PDR = k \times Mr \times \left[\frac{\sum_{i=0}^{n} (C - \bar{C})(T - \bar{T})}{\sum_{i=0}^{n} (T - \bar{T})} \Big/ Sw \right] \times \rho \times D$$

C and T are the known values of C (C0, C1, C2) and T (T0, T1 and T2), whereas $\bar{C}$ is the mean value of C0, C1, C2, and $\bar{T}$ is the mean value of T0, T1 and T2. C0, C1 and C2 were calculated as μg N_2O = μg N_2O/mL× [vol. of gas in mL +(vol. of water in mL× Bunsen Coefficient)].

PDR is the rate of potential denitrification (mg N_2O-Nm^{-2} h^{-1}), C0 is the N_2O mass at 30 min (μg N_2O-N), C1 is the N_2O mass at 60 min (μg N_2O-N), and C2 is the N_2O mass at 90 min (μg N_2O-N). k is the conversion factor (μgcm^{-2} to mgm^{-2}) = 10, M_r is the mass ratio of N_2 to N_2O (0.64), S_w is sample weight (g), ρ is bulk density (g/cm^3), D is the depth of collected sediment samples (5 cm) and T0, T1, and T2 are the durations of incubation (h).

2.2.3. Classification of LULC and accuracy assessment

Two segments of Sentinel-2B images during the dry period (11 February 2020) were downloaded (https://scihub.copernicus.eu/) and used to map LULC types. The image processing and analysis were performed using the semi-automatic classification plugin (SCP) tool in QGIS (Congedo, 2021). After collecting Sentinel-2 Level 1C products, an atmospheric correction was applied (Dark Object Subtraction, DOS1; Moran et al., 1992). To create a training set for the LULC classification, field-based observed LULC types were used. About 70 % of the polygons were used as training data and the remainder as test data for the accuracy assessment. The training data were corrected by observing the NDVI value (calculated using bands 4 and 8) during post-monsoon and pre-monsoon with spatial resolution of 10 m. Next, the random forest classification algorithm (Breiman, 2001) was applied using the ESA SNAP tool (SNAP version 8, http://step.esa.int). The Random Forest tool permits classifying a band set (10 Sentinel-2 bands except bands 1, 9, and 10 with spatial resolution varying from 10 to 20 m) using the ROI polygons in the training input. The ROIs were identified by Class IDs, and they were assigned to land use and land cover classes through Macro class IDs (https://fromgistors.blogspot.com/2021/02/random-forest-classification-using-scp.html). The accuracy of the LULC classification was assessed based on the confusion matrix, user's accuracy, producer's accuracy, overall accuracy and kappa hat coefficient values.

2.2.4. Data analysis

2.2.4.1. Differences in PDR by depth and LULC. A paired *t*-test was performed to compare the measured PDR from 0 to 5 cm depth and 5–10 cm depth. As there was no significant difference between the depths, data of 0–5 cm depth were used for the analysis. A Kruskal-Wallis rank test was applied to compare the PDR among the LULC types, with a post-hoc Dunn test with Bonferroni correction (R package "dunn.test"). All the above analyses were performed in R version 4.1.2 (R core Team, 2021).

2.2.4.2. Development of linear mixed models (LMMs). In order to develop an effective model for predicting PDR from satellite data, we first developed best-fit multivariate models using field data that relied on soil moisture and vegetation parameters. These models (defined in this paper as models F) were then modified by substituting satellite data products for field data, either partly (models FS) or completely (models S). The resulting models predicted PDR for the entire study reach.

All models were linear mixed models (LMMs) developed following the procedure described by Zuur et al. (2007, 2009). This procedure includes a series of steps starting with a conventional regression model with the best possible fit, and extending this model with random effects and variance structures to further improve the fit of the model. The best-fit model is selected based on the Akaike Information Criterion (AIC) and log-likelihood (logLik) (Sakamoto et al., 1986).

2.2.4.2.1. LMMs based on field observation (Model F). First, a linear covariance model was developed with PDR (10 log-transformed) as the dependent variable and soil moisture, vegetation cover, bulk density, LULC and elevation as independent variables (Model F-0)

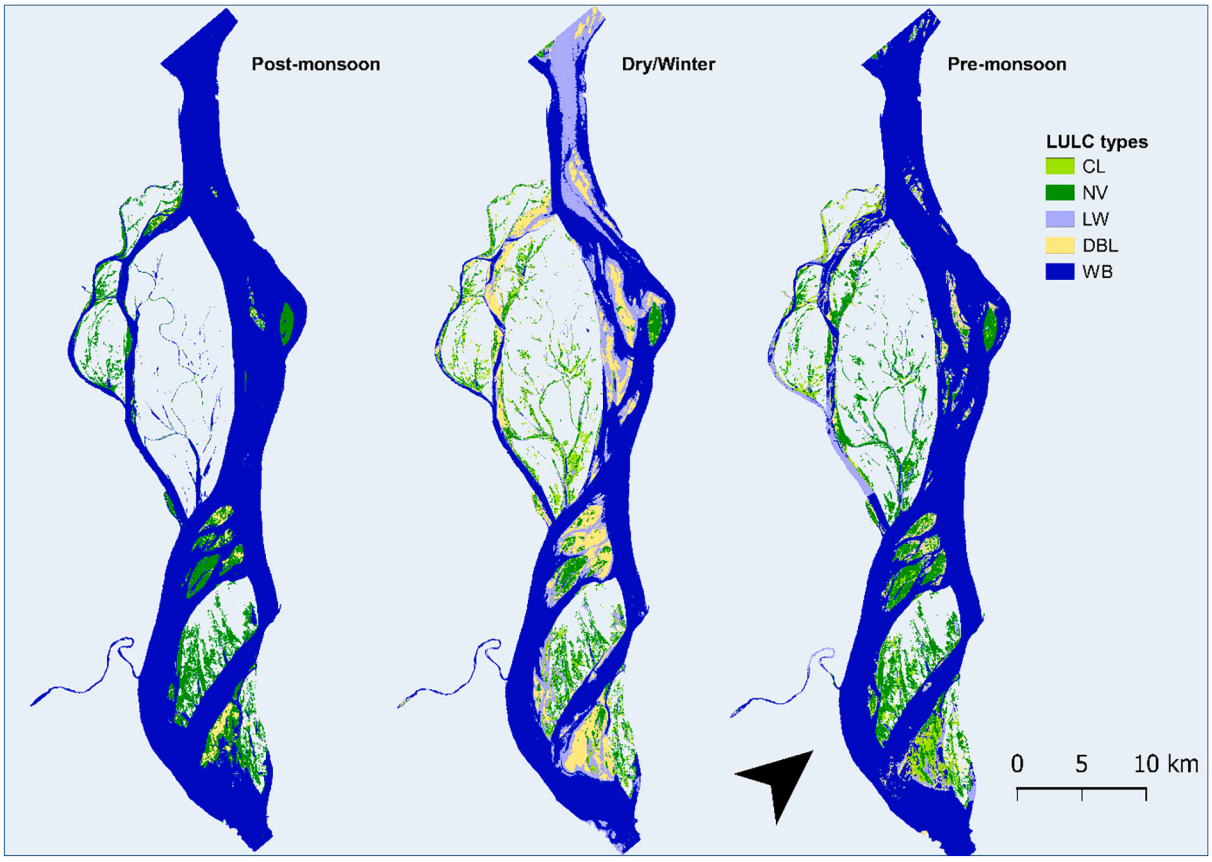

Fig. 3. LULC types of the study area of the Padma River, Bangladesh, during post-monsoon 2019, dry/winter 2020 and pre-monsoon 2020 (CL = Cropland, NV = Natural vegetation, LW = Land with water, DBL = Dry bare land and WB=Water bodies).

(Supplementary Table 1). Variables to retain in the model were selected based on the amount of variance explained by the R^2 and the significance of intercept and slope in the model estimation. To avoid multicollinearity, Pearson correlation coefficients were calculated to avoid including correlated variables in the model, and a variance inflation factor ("vif") test was conducted between the predictor variables.

Next, the model F-0 was re-analysed with a generalised least-squares model fitted by the restricted maximum likelihood method (REML) using the same independent variables (Model F-1). This model was extended with LULC as random effect (Model F-2, random intercept model) or a variance term allowing separate variances for each LULC type (Model F-3, VarIdent model). The fourth (Model F-4) combined the random intercept and the variance structure (Supplementary Table 2). The functions "gls" and "lme" (nlme package; Pinheiro et al., 2021) in R were used to run all the models.

2.2.4.2.2. Replacing field variables with satellite data (Model FS). For the selection of satellite-based variables, we calculated correlation between 12 Sentinel 2-derived bands and 35 indices and the best-fit field-based variables derived from the model F (Supplementary Table 3a, b). The Sentinel-2 band 11 and NDVI were correlated most strongly to SM and VC, respectively, and were used as fixed variables in the A models, resulting in models FS-1, FS-2, FS-3 and FS-4 (Supplementary Table 1). Field-observed LULC was retained as a random variable in the FS models.

2.2.4.2.3. LMMs with solely satellite data (Model S). The third model type was developed solely with satellite data. Satellite-derived LULC was used as a random variable instead of field-based LULC, and the models termed S-1, S-2, S-3 and S-4 (Supplementary Table 2). The same satellite-derived indices used in the S models were used as fixed variables.

2.2.4.2.4. Effects plots and model comparison. To visualise the effect of the predictor variables, effect plots were produced for all models (F, FS, S) using the R package "effects". Effect plots show the change in PDR caused by one predictor variable while assuming the average value for the other predictors. The Model II regression was performed between models measured PDR and F-4 and also, F-4 and FS-4/S-4 using the "lmodel2" package in R to evaluate modelling results (Jensen, 1986).

2.2.4.3. Preparation of raster data for model application. The resulting LULC raster data were clipped to the pre-classified NREGUs vector data to get the LULC relevant for nitrogen retention/export. After that, NDVI was calculated and clipped with LULC raster data. Sentinel-2 band 11 was also clipped to get the desired area of interest.

2.2.4.4. Model application (upscaling). The best-fit LMM (Model C4) was applied to each pixel of the NREGUs of the study area. The pixel size was 10 × 10 m, and the obtained pixels for the NREGUs in post-monsoon, dry/winter and pre-monsoon were 3665373, 3832900 and 3822060, respectively. To perform model simulation across all pixels, all the raster data were converted into spatRaster using the function "Rast" in the "terra" package in R. Then, raster data were converted to spatVector format and model computation was performed according to LULC types using the "ifelse" function in R. After that, using "rasterise" function the predicted PDR was converted into a raster file. Mapping and further analysis were done in QGIS and R, respectively.

3. Results

3.1. Classification of LULC types

The LULC types of the study area were categorized as cropland (CL), natural vegetation (NV), land with water (LW), dry, bare land (DBL) and

Table 1
The total estimated area of LULC types of the study area of Padma River during different seasons.

Class	Area (km^2)			Percentage (%)		
	Post-monsoon	Dry/ Winter	Pre-monsoon	Post-monsoon	Dry/ Winter	Pre-monsoon
CL	–	20.4	19.7	–	5.32	5.16
NV	48.1	33.6	53.5	13.1	8.77	14.0
LW	6.2	86.1	24.9	1.69	22.5	6.51
DBL	6.8	46.0	13.6	1.85	12.0	3.57
WB	305	197	270	83.3	51.5	70.8

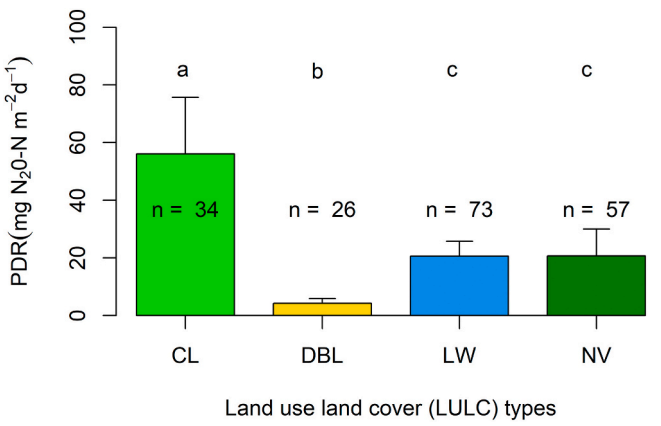

Fig. 4. Mean potential denitrification rate (PDR) in different LULC types (CL = Cropland, DBL = Dry bare land, LW = Land with water and NV=Natural vegetation) with standard error of the mean and number of samples in the study area of Padma River (Groups sharing a same letter not were significantly different ($p < 0.01$) according to Kruskal-Wallis test with a post-hoc Dunn test.

water body (WB) in all seasons except post-monsoon (Fig. 3). The land portion starts appearing in pre-monsoon, so the study area is devoid of CL. In all seasons, the area was dominated by water bodies, including primary and secondary channels, covering an area of 305, 197 and 270 km^2 during post-monsoon, dry/winter and pre-monsoon, respectively. LW, where inundation occurs for a short time, mainly comprises river edges and water depressions inside the land portion covered by about 25 % of the study area. Other LULC types, CL, NV, and DBL, covered an area of 5%, 9 % and 12 %, respectively (Table 1).

The LULC classification had a total accuracy value of 82.4 %, 87.4 % and 91.7 % and a kappa hat coefficient of 0.57, 0.7 and 0.69 during post-monsoon, dry/winter and pre-monsoon, respectively (Supplementary Table 4a, b and c).

3.2. Potential denitrification rate (PDR) in different LULC types

The measured PDR at sample sites during the dry/winter season varied from 0.41 to643mg N_2O-N$m^{-2}d^{-1}$ in CL, 0.11-523 mg N_2O-N m^{-2} d^{-1}in NV, 0.11–250 mg N_2O-N m^{-2} d^{-1}in LW and 0.07 37.72 mg N_2O-N m^{-2} d^{-1}in DBL. The highest mean value of PDR (56 mg N_2O-N m^{-2} d^{-1}) was found in CL, and the lowest mean value was in DBL (4.27 mg N_2O-N m^{-2} d^{-1}). In the case of LW and NV, the mean value of PDR was about 20 mg N_2O-N m^{-2} d^{-1} (Fig. 4). The Kruskal-Wallis test showed a significant difference of PDR among LULC types (chi-squared = 39.8, df = 3, p-value = 1.17e−8). The post-hoc Dunn's test showed that PDR in CL (group a) and DBL (group b) were significantly different from the others (Fig. 4).

3.3. Model results

The linear model with vegetation cover (VC), soil moisture (SM) and LULC had an R^2 of 0.31. In this model, the intercept, explanatory variables VC and SM, and categorical variables LULC types were significant ($p < 0.001$ or $P < 0.05$), and marginally significant for LW. The developed LMMs showed better results for models F-1 to F-4. There was a

Table 2
Comparison of different LMMs. The best-fit models with the lowest AIC and Log-likelihood values are marked in bold.

Model code	Model type	Explanatory variable source	LULC data type	AIC	Log-likelihood
F-1	Generalised least-square	Field	Field	424.49	−205.25
F-2	Random intercept	Field	Field	423.06	−206.53
F-3	Generalised least-square with variance structure	Field	Field	425.63	−205.82
F-4	Random intercept with variance structure	Field	Field	**416.31**	**−200.15**
FS-1	Generalised least-square	Satellite	Field	421.45	−203.73
FS-2	Random intercept	Satellite	Field	422.22	−206.11
FS-3	Generalised least-square with variance structure	Satellite	Field	444.49	−215.24
FS-4	Random intercept with variance structure	Satellite	Field	**418.45**	**−201.23**
S-1	Generalised least-square	Satellite	Satellite	432.18	−209.09
S-2	Random intercept	Satellite	Satellite	431.84	−210.92
S-3	Generalised least-square with variance structure	Satellite	Satellite	444.28	−215.14
S-4	Random intercept with variance structure	Satellite	Satellite	**428.52**	**−206.26**

Table 3
Results of LMMs (Models F-4, FS-4 and S-4) showing fixed effects and random effects of different factors on predicting PDR. The significance of intercepts and slopes are indicated with ** ($p < 0.01$) and *** ($p < 0.001$). The total number of observations was 190. (F = model with field-based data, FS = model with satellite and field-based data and S = model with satellite-based data).

	Model estimates					
	Model F-4		Model FS-4		Model S-4	
Fixed effects						
Intercept	−2.378	***	−1.457	***	−1.357	***
Slopes						
Veg. Cover (%)	0.0072	***				
Soil Moisture (%)	0.0348	***				
NDVI			1.356	***	1.264	**
Sentinel-2 band 11			−1.981	**	−2.271	***
Random effects						
Intercepts						
CL	0.2783		0.4564		0.3983	
DBL	−0.1773		−0.3966		−0.2820	
LW	0.0790		0.1239		0.0437	
NV	−0.1799		−0.1838		−0.1599	
Intercept stdev	0.2449		0.3873		0.3171	
Residual stdev	0.4167		0.4771		0.4794	

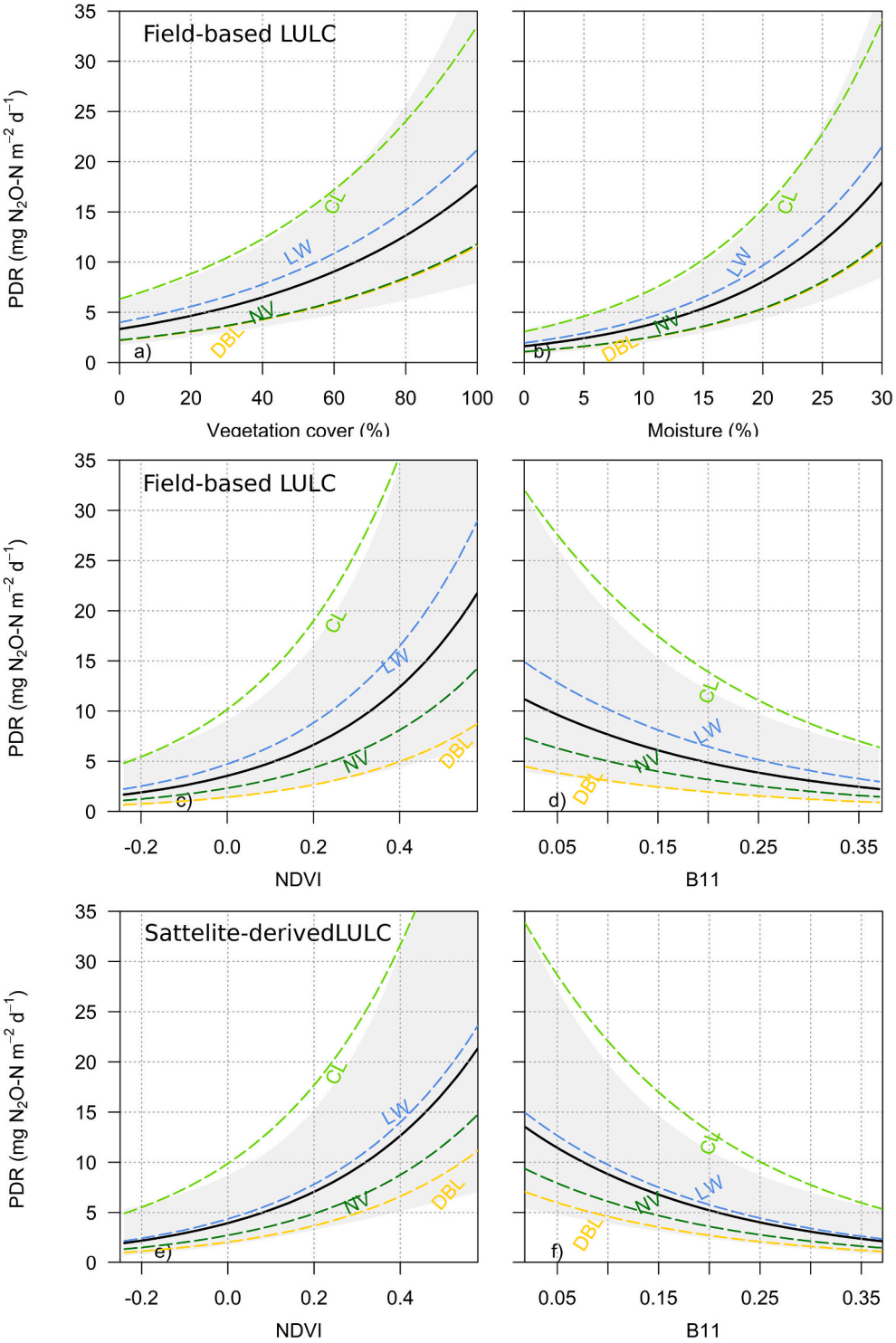

Fig. 5. Plots showing the effects of different parameters using LULC types in estimating PDR for modelsF-4, FS-4 and S-4. a, b) effect of vegetation cover and soil moisture; c, d) effect of NDVI and B11 (band 11) using field observed LULC, and e, f) same as (c, d) but with satellite-derived LULC. The bold line in the plot indicates the fixed effect of the models, and the dashed lines with different colours indicate the LULC type-specific effect of the models. The shaded area indicates the 95 % confidence interval for the mean effect value.

significant difference between models F-3 and F-4 and the lowest AIC, and the log-likelihood value indicates that model F-4 was the best for predicting PDR in the present study. Replacing VC and SM with NDVI and band 11 with field-based/satellite-based LULC types showed similar results (Model FS-1 to FS-4 and model S-1 to S-4). In all cases, the random intercept models with variance structure (Models F-4, FS-4 and S-4) showed the lowest AIC and log-likelihood values (Table 2). The explanatory variables (VC and SM) and fixed intercept were significant, and there were random effects of LULC types. The random effects showed that the highest PDR was estimated in CL, followed by LW, NV and DBL (Table 3).

For all type models (F-4, FS-4, S-4), the effect plots showed the impact of fixed variables on PDR estimation, but the magnitude of the effect differed based on LULC type (Fig. 5). CL showed an effect of higher

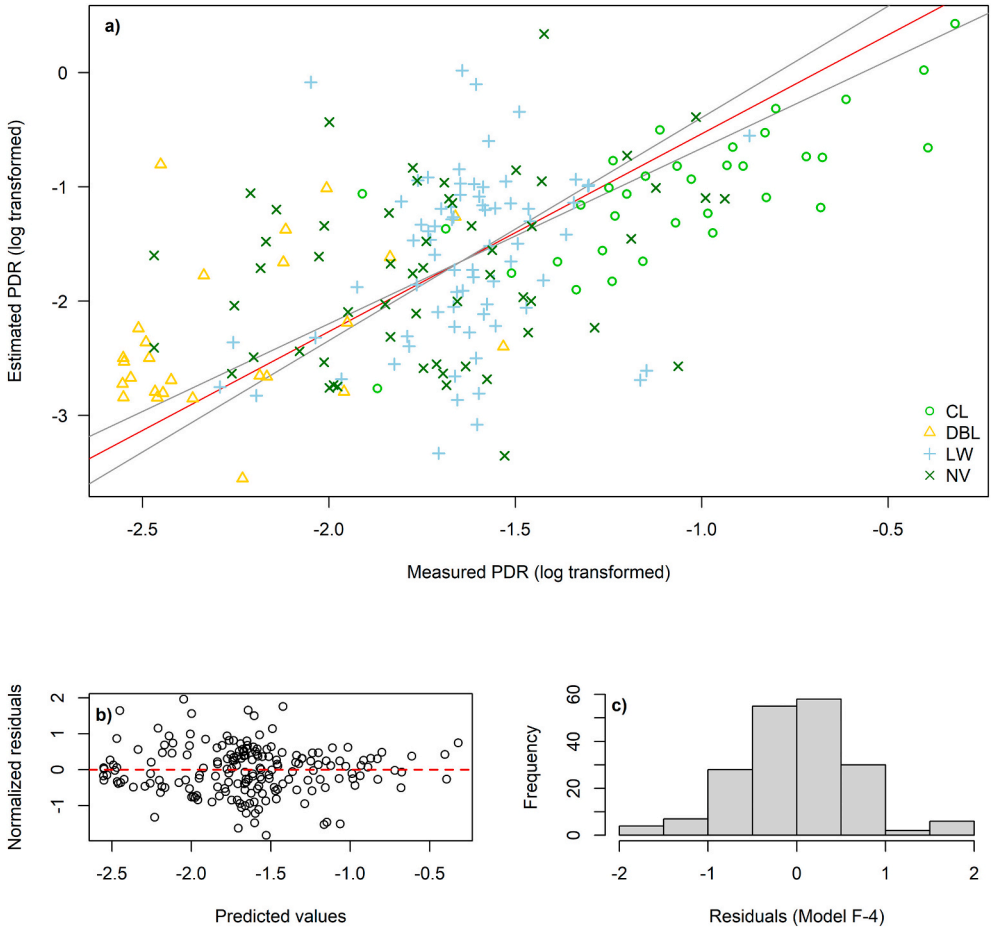

Fig. 6. a) Scatter diagram of Model F-4 fit showing regressing PDR from fixed (VC and SM) and random effects (LULC types), the diagram also showed the appropriate regression line (red line, standard major axis) with confidence intervals (2.5 % and 97.5 %) of intercepts and slopes; b) Residuals plot showing model performance (accuracy) and c) Histogram of raw residuals showing normal distribution. Coloured symbols in the plot a) represent LULC types (Cropland = light green, Natural vegetation = dark green, Land with water = blue, Dry bare land = gold).

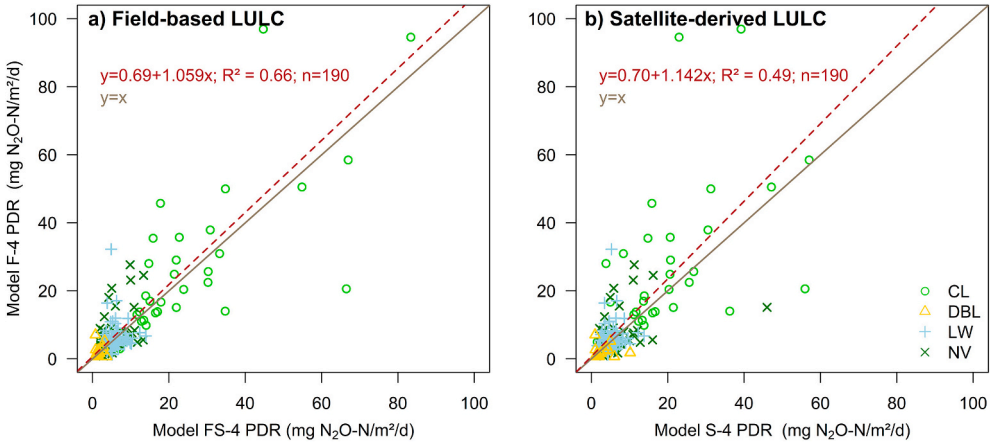

Fig. 7. Field-based (VC and SM) vs satellite-based (NDVI and band 11) estimation of PDR using field-based and satellite-derived LULC types. The dashed lines indicate the model performed estimates. The solid black line indicates the y = x line. Coloured symbols in the data represent LULC types (Cropland = light green, Natural vegetation = dark green, Land with water = blue, Dry bare land = gold).

magnitude than the other LULC types in PDR estimation, whereas DBL showed the minimum. The differences in PDR effects between NV and DBL were observed in models FS-4 and S-4, whereas in model F-4, the effects were the same (Fig. 5).

3.4. Comparison between measured and satellite estimated PDR

Fig. 6 depicts Model II regression between measured and estimated (Model-F4) PDR. The normalised residuals with few outliers indicate a relatively precise and unbiased model (Fig. 6 b and c). In Fig. 7, satellite

Table 4
Confidence intervals of the Model II regressions (Model FS-4 vs Model F-4 and Model S-4 vs Model F-4).

Regression Models	2.5 % intercept	97.5 % intercept	2.5 % slope	97.5 % slope
Model FS-4 vs Model F-4	−0.919	2.291	0.949	1.171
Model S-4 vs Model F-4	−1.364	2.764	0.974	1.309

data-estimated PDR is plotted against field data-measured PDR. Both regression lines were not significantly different from the y = x line based on the 95 % confidence interval of the slopes and intercepts (Fig. 7, Table 4. The coefficient of determination (R^2 = 0.66) indicates a good correspondence between the two datasets (i.e. field compared with satellite). This provides evidence that NDVI and band 11 can be used with sufficient reliability as a proxy for vegetation cover and soil moisture. However, when satellite-derived LULC was used, the R^2 was 0.49 (Fig. 7). This was logical because satellite-derived LULC is not as precise as field-observed LULC types.

3.5. Spatio-temporal distribution of PDR

3.5.1. Mapping of the model estimated PDR

The model estimation (model S-4) showed that PDR ranged from 0–35 mg N_2O-N m^{-2} d^{-1} during post-monsoon, 0–82.8 mg N_2O-N m^{-2} d^{-1}duringdry/winter, and 0–120 mg N_2O-N m^{-2} d^{-1} during post-monsoon (Fig. 8). An increase of modelled PDR was observed from post-monsoon 2019 to pre-monsoon, 2020. The lowest value of modelled PDR was observed in DBL during all three seasons. The higher PDR was found in the VI, where CL and NV were the dominant LULC types (Figs. 3 and 8).

3.5.2. Comparison of estimated PDR in different NREGUs

The mean estimated PDR (Model S-4) ranged from 0–10, 0–15 and 0–20 mg N_2O-N m^{-2} d^{-1} in post-monsoon, dry/winter and post-monsoon, respectively. The median value of PDR was increased from post-monsoon 2019 to pre-monsoon 2020 in all GUs except EK, in post-monsoon. In all three seasons, the highest median value was found in VI, mainly owing to CL or NV, and the lowest median PDR was found in the unvegetated bank (EK) post-monsoon as the GUs started emerging then. In WD, the median value of PDR was higher than the bars in the river (L, T and SB) except in the pre-monsoon. In this season, PDR was higher in EK and occurred due to the start of inundation (Fig. 9). An increase in the water content of EK mainly increases PDR.

3.5.2.1. Impact of GUs on PDR estimation. Estimated nitrogen lost from the study area through denitrification was 191, 1087and 972 kg N_2O-N d^{-1}during post-monsoon, dry/winter and pre-monsoon, respectively. The total PDR count in the vegetation island (VI) showed that the estimated PDR increased from post-monsoon 2019 to dry/winter 2020 and decreased in pre-monsoon 2020, associated with the increased surface area from post-monsoon to dry/winter. After that, it tended to decrease. Again, in mid bars (L and T) the surface area and the number of NREGUs increased from post-monsoon to pre-monsoon, accelerating the increasing tendency of PDR from post-monsoon to pre-monsoon, but in case of the side bar (SB), the PDR was maximum during pre-monsoon due to increase of the number of NREGUs. In the case of EK, ED and WD, the maximum surface area and the highest number were observed post-monsoon, which corresponded to the highest total estimated PDR in these NREGUs (Fig. 10).

4. Discussion

LMMs developed during this study were able to predict PDR reasonably well using independent variables of vegetation cover, soil moisture and LULC. These factors have been shown previously to have a regulating role for PDR (Xiong et al., 2017; Orr et al., 2014; Chen et al.,

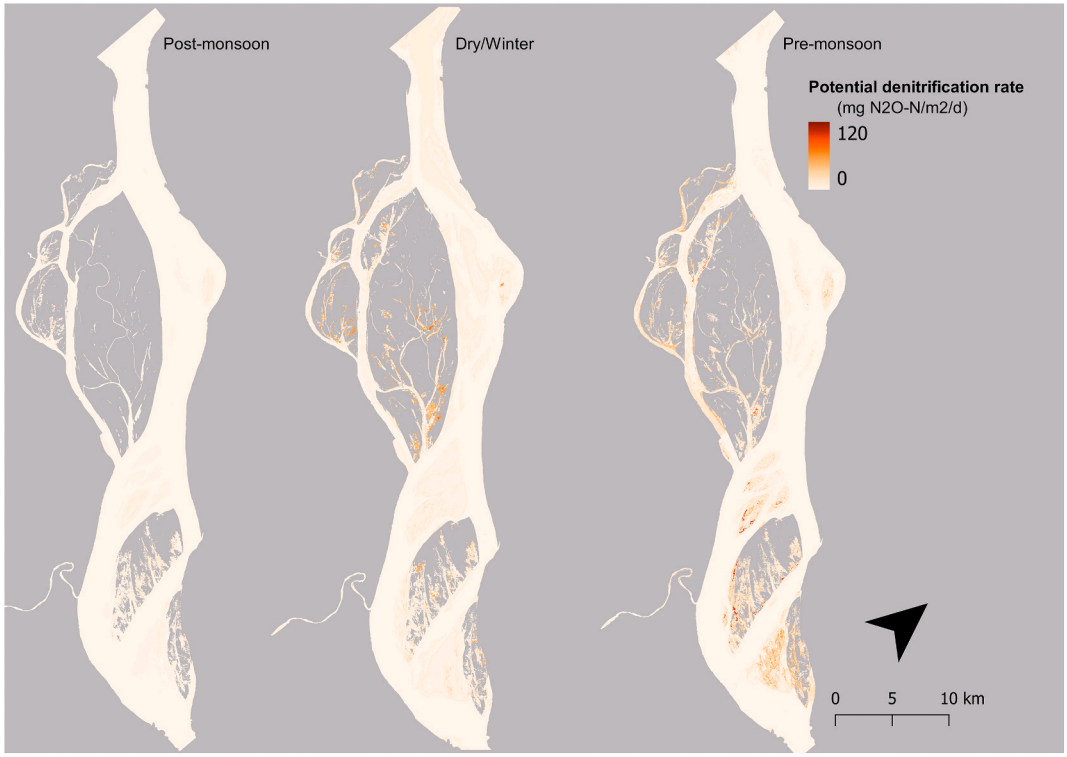

Fig. 8. Estimated PDR (potential denitrification rate) in the study area of Padma River during the post-monsoon 2019, dry/winter 2020 and pre-monsoon 2020 (WB was excluded in the estimation) based on model S-4, which relies on NDVI, band 11 and LULC. See text for further information.

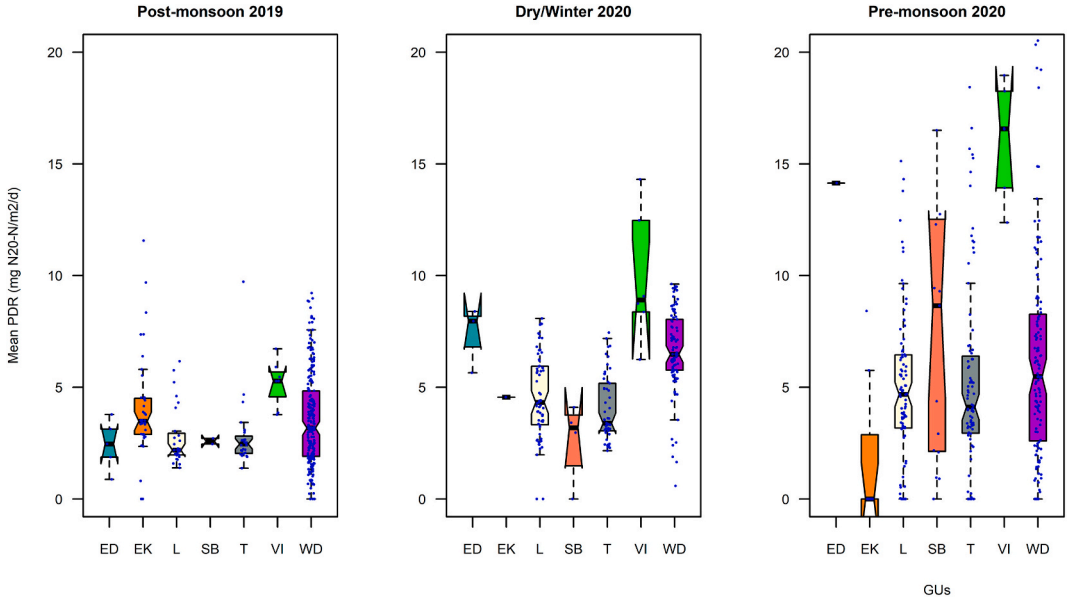

Fig. 9. Model estimated mean denitrification rate in different GUs during post-monsoon 2019, dry/winter 2020 and pre-monsoon 2020 (ED=Dry channel, EK = Unvegetated bank, L = Longitudinal bar, SB = Side bar, T = Transverse bar, VI = Vegetation Island, WD = Water depression).

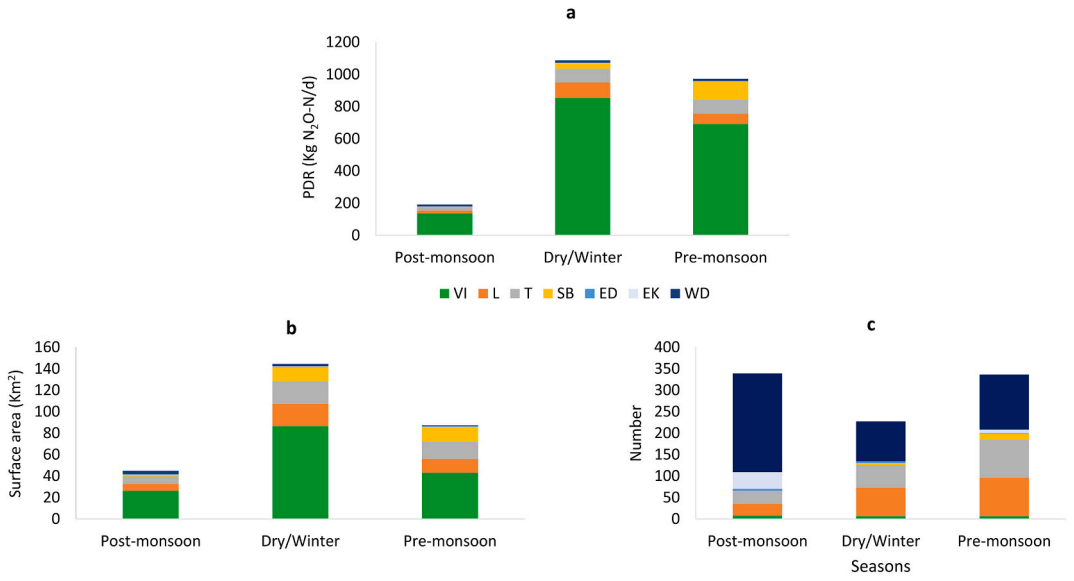

Fig. 10. Estimated PDR (a), the total surface area of GUs (b) and the number of GUs (c) during different seasons in the study area of Padma River, Bangladesh (ED=Dry channel, EK = Unvegetated bank, L = Longitudinal bar, SB = Side bar, T = Transverse bar, VI = Vegetation Island, WD = Water Depression).

2009), although PDR can vary with changes in LULC types in river systems (Korol et al., 2019; Jung et al., 2014). Satellite-derived remote sensing data enables scaling up of PDR across river reaches. The remote sensing derived NDVI provided a sufficiently robust proxy for vegetation dynamics, as we found a significant correlation between vegetation cover and NDVI. The NDVI mostly correlated with Sentinel-2-derived indexes used to determine soil moisture, butSentinel-2band 11 did not correlate significantly with NDVI. In the LMM model, a combination of these two showed better results in the model estimation than the other Sentinel-2 bands and indexes. In the dataset, LULC played a significant role in model PDR estimation providing random effects as intercepts based on LULC. The highest PDR estimated in CL was from the application of fertiliser to maximise crop production (Ahmmed et al., 2018), or the presence of legumes. PDR is commonly higher in river catchments dominated by agriculture compared with forests and natural vegetation (Welsh et al., 2017; Han et al., 2017; Liu et al., 2016).

As seasonal discharge affects the surface area of classified nutrient retention or export relevant geomorphic units (NREGUs) in the study area (Gani et al., 2022), it is likely also influential for altering PDR from post-monsoon 2019 to pre-monsoon 2020, supplying nitrogen through infiltrating river water and deposited river sediment that supported vegetation growth. The nature of the NREGUs also contributed to PDR. During pre-monsoon, both in CL and NV vegetation were in a seasonally mature stage, so the highest mean PDR was observed in that period due to the higher value of NDVI. On the other hand, the lowest mean PDR occurred post-monsoon because the plants just started growing as the islands and bars began appearing. In addition, the cultivation of CL throughout the year, except for post-monsoon, had an impact on the spatiotemporal distribution of PDR.

The present study area is comparable with floodplain areas or

riparian zones where inundation occurs temporally, accelerating the enrichment of nitrogen in NREGUs (Xiong et al., 2017; Koschorreck and Darwich, 2003). The nitrate concentration of inundating waters is one of the factors that control denitrification (Ma et al., 2020; Orr et al., 2014). The study area also acts as a buffer zone for nitrate concentration, especially when water interacted with the edges of NREGUs. During the present study, we found the total maximum PDR during dry/winter due to surface area, but the mean value of PDR was the highest in all NREGUs during pre-monsoon. During this time, river discharge tends to increase, so the edge of all NREGUs becomes saturated with water, creating anoxic condition that are needed for denitrification (Seitzinger et al., 2006). It was not possible to show the influence of nitrogen inputs via river water and deposited sediments during the present study in the case of individual NREGUs separately, but the impact of the number of bars (SB) and dry channels (ED) and unvegetated banks (EK) on PDR estimation during post-monsoon and pre-monsoon showed that increasing tendency of water connectivity, i.e. inundation frequency with the bars increases microbial activity (Fischer et al., 2005). Hence, PDR increased in pre-monsoon and post-monsoon for these types of NREGUs. Such a phenomenon was observed in the case of N_2O emissions (indicative of PDR) in the White River vegetation (Jacinthe et al., 2012) and in the Congo River basin (Borges et al., 2019), where flood frequency or wetland connectivity increased the denitrification rate. There might be other factors responsible for accelerating PDR during pre-monsoon. Recent studies showed that high temperatures could influence denitrification in lowland rivers (Gervasio et al., 2022; Ding et al., 2019). During pre-monsoon, the area experienced higher temperatures than the other seasons, which likely contributed to a higher mean value of PDR.

The measurement of PDR is based on the denitrification enzyme activity (DEA), which estimates the denitrifier population in soils that is reflective of long-term in situ denitrification rates (Tiedje et al., 1982). So, the present model estimated PDR as a proxy for actual denitrification. Measuring the actual denitrification rate for large rivers with high discharge is challenging, where access to sampling sites is difficult (Boyer et al., 2006; Groffman et al., 2006). Even though possible, applying the small-scale field measurements to the riverscape scale is more challenging owing to the considerable variability of environmental factors and spatial distribution (Orr et al., 2014; Martínez-Espinosa et al., 2021). Considering this, the modelling we used provides an alternative approach for estimating the denitrification rate and scaling up to the larger reach of basin scales.

Denitrification is one of the key retention processes in large rivers, but due to methodological difficulties, its quantification has been largely limited to point locations. Previous studies have been unable to realistically and representatively map the spatiotemporal distribution of denitrification. At reach or even larger scales, denitrification is mainly controlled by nitrogen flux and water residence time, which is influenced by river discharge and GUs. Considering this interaction between hydrology and geomorphology in large tropical rivers, the current approach can be more effective. The model can estimate denitrification from very local to large-scale because PDR is calculated in the model pixel to pixel and reported per day. Moreover, the use of Sentinel-2 data provides the opportunity to predict PDR on finer time scales (the global revisit time of Sentinel-2 is five days) with higher resolution (20 m). Therefore, the present modelling is a parsimonious tool that can provide a more precise temporal estimation.

We expect this satellite-based model is applicable to any river system with temporary inundation. But to apply this model, a potential area of nutrient retention must be identified, as described by Gani et al. (2022), and LULC types should be classified more precisely. There are other limitations of the model. We validated the model with field data for only one season. Due to the highly dynamic and flooding nature of the river, it was not possible to collect samples in other seasons. This constraint can be overcome by validating this model in other river systems. Due to the cloud cover of the study area, we were only able to show the PDR estimation on a seasonal basis, but this can be done monthly based on the availability of satellite products.

5. Conclusion

In the present study, the importance of soil moisture, vegetation, and LULC as the drivers of PDR was determined by the use of linear mixed models. The developed model showed the spatiotemporal distribution of PDR using Sentinel-2 data at reach scale and could explain reasonably well the role of NREGUs in PDR on spatial and seasonal scales in the study area. The vegetation islands and the bars were the most important GUs for denitrification in all seasons. Together with the surface area, the number of NREGUs, LULC and river discharge was also responsible for the spatiotemporal distribution of PDR. The present research is a novel approach that uses satellite products to estimate PDR and can be applied to the GUs in large lowland rivers where inundation occurs frequently.

CRediT authorship contribution statement

Md Ataul Gani: Writing – original draft, Visualization, Software, Methodology, Investigation, Formal analysis, Data curation, Conceptualization. **Anne A. van Dam:** Writing – review & editing, Visualization, Software, Methodology, Formal analysis. **Johannes van der Kwast:** Writing – review & editing, Visualization, Supervision, Software. **Michael E. McClain:** Writing – review & editing, Supervision. **Kenneth A. Irvine:** Writing – review & editing, Supervision. **Gretchen M. Gettel:** Writing – review & editing, Supervision, Methodology, Formal analysis, Data curation, Conceptualization.

Funding sources

Financial support was provided by the Ministry of Science and Technology, The Government of the People's Republic of Bangladesh.

Declaration of competing interest

The authors declare no competing interests.

Acknowledgements

The authors are grateful to the research students at Jagannath University, Dhaka, Bangladesh, for their help during field sampling and lab analysis.

Appendix A. Supplementary data

Supplementary data to this article can be found online at https://doi.org/10.1016/j.scitotenv.2024.178287.

Data availability

Data will be made available on request.

References

Ahmmed, S., Jahiruddin, M., Razia, S., Begum, R.S., Biswas, J.S., Rahman, A.S.M.M., Ali, M.M., Islam, K.M.S., Hossain, M.M., Gani, M.N., Hossain, G.M.A., Sultan, M.A., 2018. Fertilizer Recomendation Guide-2018. Bangladesh Agricultural Research Council (BARC), Farmgate, Dhaka 1215.

Alexander, R.B., Smith, R.A., Schwarz, G.E., 2000. Effect of stream channel size on the delivery of nitrogen to the Gulf of Mexico. Nature 403 (6771), 758–761. https://doi.org/10.1038/35001562.

Audet, J., Olsen, T.M., Elsborg, T., Baattrup-Pedersen, A., Riis, T., 2021. Influence of plant habitats on denitrification in lowland agricultural streams. J. Environ. Manage. 286. https://doi.org/10.1016/j.jenvman.2021.112193.

Bai, J., Ouyang, H., Deng, W., Zhu, Y., Zhang, X., Wang, Q., 2005. Spatial distribution characteristics of organic matter and total nitrogen of marsh soils in river marginal wetlands. Geoderma 124 (1–2), 181–192. https://doi.org/10.1016/j.geoderma.2004.04.012.

Beaulieu, J.J., Tank, J.L., Hamilton, S.K., Wollheim, W.M., Hall, R.O., Mulholland, P.J., Peterson, B.J., Ashkenas, L.R., Cooper, L.W., Dahm, C.N., Dodds, W.K., Grimm, N.B., Johnson, S.L., McDowell, W.H., Poole, G.C., Maurice Valett, H., Arango, C.P., Bernot, M.J., Burgin, A.J., Thomas, S.M., 2011. Nitrous oxide emission from denitrification in stream and river networks. Proc. Natl. Acad. Sci. U. S. A. 108 (1), 214–219. https://doi.org/10.1073/pnas.1011464108.

Böhlke, J.K., Harvey, J.W., Voytek, M.A., 2004. Reach-scale isotope tracer experiment to quantify denitrification and related processes in a nitrate-rich stream, midcontinent United States. Limnol. Oceanogr. 49 (3), 821–838. https://doi.org/10.4319/lo.2004.49.3.0821.

Borges, A.V., Darchambeau, F., Lambert, T., Morana, C., Allen, G.H., Tambwe, E., ToengahoSembaito, A., Mambo, T., Wabakhangazi, J.N., Descy, J.P., Teodoru, C.R., Bouillon, S., 2019. Variations in dissolved greenhouse gases (CO2, CH4, N2O) in the Congo River network overwhelmingly driven by fluvial-wetland connectivity. Biogeosciences 16 (19), 3801–3834. https://doi.org/10.5194/bg-16-3801-2019.

Boyer, E.W., Alexander, R.B., Parton, W.J., Li, C., Butterbach-Bahl, K., Donner, S.D., Skaggs, R.W., Del Grosso, S.J., 2006. Modelingdenitrification in terrestrial and aquatic ecosystems at regional scales. Ecological Applications 16 (6), 2123–2142. https://doi.org/10.1890/1051-0761(2006)016[2123:MDITAA]2.0.CO;2.

Breiman, L., 2001. Random forests. Mach. Learn. 45, 5–32. https://doi.org/10.1023/A:1010933404324.

Chen, F., Jia, G., Chen, J., 2009. Nitrate sources and watershed denitrification inferred from nitrate dual isotopes in the Beijiang River, south China. Biogeochemistry 94 (2), 163–174. https://doi.org/10.1007/s10533-009-9316-x.

Cho, H.J., Kirui, P., Natarajan, H., 2008. Test of multi-spectral vegetation index for floating and canopy-forming submerged vegetation. Int. J. Environ. Res. Public Health 5 (5), 477–483.

Congedo, L., 2021. Semi-automatic classification plugin: a Python tool for the download and processing of remote sensing images in QGIS. Journal of Open Source Software 6 (64), 3172. https://doi.org/10.21105/joss.03172.

Dai, Q., Cui, C. feng, Wang, S., 2022. Spatiotemporal variation and sustainability of NDVI in the Yellow River basin. Irrigation and Drainage 1–15. https://doi.org/10.1002/ird.2740.

Davidson, E.A., Seitzinger, S., 2006. The enigma of progress in denitrification research. Ecological Applications 16 (6), 2057–2063. https://doi.org/10.1890/1051-0761(2006)016[2057:TEOPID]2.0.CO;2.

Ding, J., Xi, B., Xu, Q., Meng, H., Shen, Y., Cheng, H., 2019. Isotopic evidence of nitrate sources and its transformations in a human-impacted watershed. Environmental Science: Processes and Impacts 21 (3), 575–583. https://doi.org/10.1039/c8em00424b.

Fischer, H., Kloep, F., Wilzcek, S., Pusch, M.T., 2005. A river's liver - microbial processes within the hyporheic zone of a large lowland river. Biogeochemistry 76 (2), 349–371. https://doi.org/10.1007/s10533-005-6896-y.

Gani, M.A., van der Kwast, J., McClain, M.E., Gettel, G., Irvine, K., 2022. Classification of geomorphic units and their relevance for nutrient retention or export of a large lowland Padma River, Bangladesh: a NDVI based approach. Remote Sens. (Basel) 14 (6). https://doi.org/10.3390/rs14061481.

Garnier, J.A., Mounier, E.M., Laverman, A.M., Billen, G.F., 2010. Potential denitrification and nitrous oxide production in the sediments of the Seine River drainage network (France). J. Environ. Qual. 39 (2), 449–459. https://doi.org/10.2134/jeq2009.0299.

Gervasio, M.P., Soana, E., Granata, T., Colombo, D., Castaldelli, G., 2022. An unexpected negative feedback between climate change and eutrophication: higher temperatures increase denitrification and buffer nitrogen loads in the Po River (northern Italy). Environ. Res. Lett. 17 (8). https://doi.org/10.1088/1748-9326/ac8497.

Groffman, P.M., Axelrod, E.A., Lemunyon, J.L., Sullivan, W.M., 1991. Denitrification in grass and forest vegetated filter strips. J. Environ. Qual. 20 (3), 671–674. https://doi.org/10.2134/jeq1991.00472425002000030027x.

Groffman, P.M., Holland, E.A., Myrold, D.D., Robertson, G.P., Z., X., 1999. Denitrification. In: Robertson G. P., S.P., Coleman, D.C., Bledose, C.S. (Eds.), Standard Soil Methods for Long-term Ecological Research. Oxford University Press, pp. 272–288.

Groffman, P.M., Altabet, M.A., Böhlke, J.K., Butterbach-Bahl, K., David, M.B., Firestone, M.K., Giblin, A.E., Kana, T.M., Nielsen, L.P., Voytek, M.A., 2006. Methods for measuring denitrification: diverse approaches to a difficult problem. Ecol. Appl. 16 (6), 2091–2122. https://doi.org/10.1890/1051-0761(2006)016[2091:MFMDDA]2.0.CO;2.

Guilhen, J., Al Bitar, A., Sauvage, S., Parrens, M., Martinez, J.M., Abril, G., Moreira-Turcq, P., Sanchez-Perez, J.M., 2020. Denitrification and associated nitrous oxide and carbon dioxide emissions from the Amazonian wetlands. Biogeosciences 17 (16), 4297–4311. https://doi.org/10.5194/bg-17-4297-2020.

Guo, X., Fu, Q., Hang, Y., Lu, H., Gao, F., Si, J., 2020. Spatial variability of soil moisture in relation to land use types and topographic features on hillslopes in the black soil (mollisols) area of Northeast China. Sustainability 12 (9), 3552. https://doi.org/10.3390/su12093552.

Gupta, A., 2007. Greatest floods and largest rivers. In: Large Rivers: Geomorphology and Management. https://doi.org/10.1002/9780470723722.

Han, L., Huang, W., Yuan, X., Zhao, Y., Ma, Z., Qin, J., 2017. Denitrification potential and influencing factors of the riparian zone soils in different watersheds, Taihu Basin. Water Air Soil Pollut. 228 (3). https://doi.org/10.1007/s11270-017-3287-7.

Hansen, A.T., Dolph, C.L., Finlay, J.C., 2016. Do wetlands enhance downstream denitrification in agricultural landscapes? Ecosphere 7 (10), e01516. https://doi.org/10.1002/ecs2.1516.

Hoang, L., van Griensven, A., Mynett, A., 2017. Enhancing the SWAT model for simulating denitrification in riparian zones at the river basin scale. Environ. Model. Softw. 93, 163–179. https://doi.org/10.1016/j.envsoft.2017.03.017.

Holzman, M.E., Rivas, R.E., Bayala, M.I., 2021. Relationship between tir and nir-swir as indicator of vegetation water availability. Remote Sensing 13 (17). https://doi.org/10.3390/rs13173371.

Jacinthe, P.A., Bills, J.S., Tedesco, L.P., Barr, R.C., 2012. Nitrous oxide emission from riparian buffers in relation to vegetation and flood frequency. J. Environ. Qual. 41 (1), 95–105. https://doi.org/10.2134/jeq2011.0308.

Jensen, A.L., 1986. Functions regression and correlation Ana. Can. J. Fish. Aquat. Sci. 43, 6–9.

Jung, S.P., Kim, Y.J., Kang, H., 2014. Denitrification rates and their controlling factors in streams of the Han River basin with different land-use patterns. Pedosphere 24 (4), 516–528. https://doi.org/10.1016/S1002-0160(14)60038-2.

Kaden, U.S., Fuchs, E., Geyer, S., Hein, T., Horchler, P., Rupp, H., Scholz, M., Schulz-Zunkel, C., Weigelhofer, G., 2021. Soil characteristics and hydromorphological patterns control denitrification at the floodplain scale. Front. Earth Sci. 9. https://doi.org/10.3389/feart.2021.708707.

Korol, A.R., Noe, G.B., Ahn, C., 2019. Controls of the spatial variability of denitrification potential in nontidal floodplains of the Chesapeake Bay watershed, USA. Geoderma 338, 14–29. https://doi.org/10.1016/j.geoderma.2018.11.015.

Koschorreck, M., Darwich, A., 2003. Nitrogen dynamics in seasonally flooded soils in the Amazon floodplain. Wetl. Ecol. Manag. 11 (5), 317–330. https://doi.org/10.1023/B:WETL.0000005536.39074.72.

Kreiling, R.M., Richardson, W.B., Bartsch, L.A., Thoms, M.C., Christensen, V.G., 2019. Denitrification in the river network of a mixed land use watershed: unpacking the complexities. Biogeochemistry 143 (3), 327–346. https://doi.org/10.1007/s10533-019-00565-6.

Laursen, A.E., Seitzinger, S.P., 2002. Measurement of denitrification in rivers: an integrated, whole reach approach. Hydrobiologia 485, 67–81. https://doi.org/10.1023/A:1021398431995.

Lin, J., Chen, N., Wang, F., Huang, Z., Zhang, X., Liu, L., 2020. Urbanization increased river nitrogen export to western Taiwan Strait despite increased retention by nitrification and denitrification. Ecol. Indic. 109, 105756. https://doi.org/10.1016/j.ecolind.2019.105756.

Liu, W., Xiong, Z., Liu, H., Zhang, Q., Liu, G., 2016. Catchment agriculture and local environment affecting the soil denitrification potential and nitrous oxide production of riparian zones in the Han River basin, China. Agric. Ecosyst. Environ. 216, 147–154. https://doi.org/10.1016/j.agee.2015.10.002.

Ma, L., Xiong, Z., Yao, L., Liu, G., Zhang, Q., Liu, W., 2020. Soil properties alter plant and microbial communities to modulate denitrification rates in subtropical riparian wetlands. Land Degrad. Dev. 31 (14), 1792–1802. https://doi.org/10.1002/ldr.3569.

Maavara, T., Lauerwald, R., Laruelle, G.G., Akbarzadeh, Z., Bouskill, N.J., Van Cappellen, P., Regnier, P., 2019. Nitrous oxide emissions from inland waters: are IPCC estimates too high? Glob. Chang. Biol. 25 (2), 473–488. https://doi.org/10.1111/gcb.14504.

Martínez-Espinosa, C., Sauvage, S., Al Bitar, A., Green, P.A., Vörösmarty, C.J., Sánchez-Pérez, J.M., 2021. Denitrification in wetlands: a review towards a quantification at global scale. Sci. Total Environ. 754, 142398. https://doi.org/10.1016/j.scitotenv.2020.142398.

Martínez-Espinosa, C., Sauvage, S., Al Bitar, A., Sánchez Pérez, J.M., 2022. A dynamic model for assessing soil denitrification in large-scale natural wetlands driven by Earth Observations. Environ. Model. Software 158, 105557. https://doi.org/10.1016/J.ENVSOFT.2022.105557.

Moran, M.S., Jackson, R.D., Slater, P.N., Teillet, P.M., 1992. Evaluation of simplified procedures for retrieval of land surface reflectance factors from satellite sensor output. Remote Sens. Environ. 41 (2–3), 169–184. https://doi.org/10.1016/0034-4257(92)90076-V.

Nanus, L., Williams, M.W., Campbell, D.H., Elliott, E.M., Kendall, C., 2008. Evaluating regional patterns in nitrate sources to watersheds in national parks of the rocky mountains using nitrate isotopes. Environ. Sci. Tech. 42 (17), 6487–6493. https://doi.org/10.1021/es800739e.

Nilsson, J.E., Liess, A., Ehde, P.M., Weisner, S.E.B., 2020. Mature wetland ecosystems remove nitrogen equally well regardless of initial planting. Sci. Total Environ. 716, 137002. https://doi.org/10.1016/j.scitotenv.2020.137002.

Opdyke, M.R., David, M.B., Rhoads, B.L., 2006. Influence of geomorphological variability in channel characteristics on sediment denitrification in agricultural streams. J. Environ. Qual. 35 (6), 2103–2112. https://doi.org/10.2134/jeq2006.0072.

Orr, C.H., Predick, K.I., Stanley, E.H., Rogers, K.L., 2014. Spatial autocorrelation of denitrification in a restored and a natural floodplain. Wetlands 34 (1), 89–100. https://doi.org/10.1007/s13157-013-0488-8.

Peng, J., Albergel, C., Balenzano, A., Brocca, L., Cartus, O., Cosh, M.H., Crow, W.T., Dabrowska-Zielinska, K., Dadson, S., Davidson, M.W.J., de Rosnay, P., Dorigo, W., Gruber, A., Hagemann, S., Hirschi, M., Kerr, Y.H., Lovergine, F., Mahecha, M.D., Marzahn, P., Loew, A., 2021. A roadmap for high-resolution satellite soil moisture applications – confronting product characteristics with user requirements. Remote Sens. Environ. 252, 112162. https://doi.org/10.1016/j.rse.2020.112162.

Piña-Ochoa, E., Álvarez-Cobelas, M., 2006. Denitrification in aquatic environments: a cross-system analysis. Biogeochemistry 81 (1), 111–130. https://doi.org/10.1007/s10533-006-9033-7.

Pinheiro, J., Bates, D., DebRoy, S., Sarkar, D., T., R.C., 2021. nlme: Linear and Nonlinear Mixed Effects Models (3.1-152). https://CRAN.R-project.org/package=nlme.

Pribyl, A.L., McCutchan, J.H., Lewis, W.M., Saunders, J.F., 2005. Whole-system estimation of denitrification in a plains river: a comparison of two methods. Biogeochemistry 73 (3), 439–455. https://doi.org/10.1007/s10533-004-0565-4.

Rinaldi, M., Belletti, B., Comiti, F., Nardi, L., Bussettini, M., Mao, L., M., G.A., 2015. Deliverable 2.1, Part 1, of REFORM (REstoring rivers FOR effective catchment

Management), a Collaborative project (large-scale integrating project) funded by the European Commission within the 7th Framework Programme under Grant Agreement 282656 (Issue November).
Ritz, S., Fischer, H., 2019. A mass balance of nitrogen in a large lowland river (Elbe, Germany). Water 11 (11), 2383. https://doi.org/10.3390/w11112383.
Ritz, S., Dähnke, K., Fischer, H., 2018. Open-channel measurement of denitrification in a large lowland river. Aquat. Sci. 80 (1), 1–13. https://doi.org/10.1007/s00027-017-0560-1.
Robertson, K., Klemedtsson, L., Axelsson, S., Rosswall, T., 1993. Estimates of denitrification in soil by remote sensing of thermal infrared emission at different moisture levels. Biol. Fertil. Soils 16 (3), 193–197. https://doi.org/10.1007/BF00361407.
Sakamoto, Y., Ishiguro, M., Kitagawa, G., 1986. Akaike Information Criterion Statistics. D. Reidel Publishing Company.
Sebilo, M., Billen, G., Grably, M., Mariotti, A., 2017. Isotopic composition of nitrate-nitrogen as a marker of riparian and benthic denitrification at the scale of the whole seine river system. Author (s): Mathieu Sebilo, Gilles Billen, MichelineGrably and André Mariotti Published by: Springer Stable URL Biogeochemistry 63 (1), 35–51.
Seitzinger, S.P., Styles, R.V., Boyer, E.W., Alexander, R.B., Billen, G., Howarth, R.W., M., B., B., N.V., 2002. The nitrogen cycle at regional to global scales. In: Boyer, E.W., Howarth, R.W. (Eds.), The Nitrogen Cycle at Regional to Global Scales. Springer, Netherlands, pp. 199–237. https://doi.org/10.1007/978-94-017-3405-9.
Seitzinger, S., Harrison, J.A., Böhlke, J.K., Bouwman, A.F., Lowrance, R., Peterson, B., Tobias, C., van Drecht, G., 2006. Denitrification across landscapes and waterscapes: a synthesis. Ecol. Appl. 16 (6), 2064–2090. https://doi.org/10.1890/1051-0761(2006)016[2064:DALAWA]2.0.CO;2.
Sgouridis, F., Ullah, S., 2014. Denitrification potential of organic, forest and grassland soils in the Ribble-Wyre and Conwy River catchments, UK. Environmental Sciences: Processes and Impacts 16 (7), 1551–1562. https://doi.org/10.1039/c3em00693j.
Shrestha, J., Niklaus, P.A., Frossard, E., Samaritani, E., Huber, B., Barnard, R.L., Schleppi, P., Tockner, K., Luster, J., 2012. Soil nitrogen dynamics in a river floodplain mosaic. J. Environ. Qual. 41 (6), 2033–2045. https://doi.org/10.2134/jeq2012.0059.
Solomon, C.T., Hotchkiss, E.R., Moslemi, J.M., Ulseth, A.J., Stanley, E.H., Hall, R.O., Flecker, A.S., 2009. Sediment size and nutrients regulate denitrification in a tropical stream. J. N. Am. Benthol. Soc. 28 (2), 480–490. https://doi.org/10.1899/07-157.1.
Sørensen, J., 1978. Denitrification rates in a marine sediment as measured by the acetylene inhibition technique. Appl. Environ. Microbiol. 36 (1), 139–143. https://doi.org/10.1128/aem.36.1.139-143.1978.
Strauss, E.A., Richardson, W.B., Bartsch, L.A., Cavanaugh, J.C., 2011. Effect of habitat type on in-stream nitrogen loss in the Mississippi River. River Syst. 19, 261–269. https://doi.org/10.1127/1868-5749/2011/019-0021.
Sun, X., Bernard-Jannin, L., Sauvage, S., Garneau, C., Arnold, J.G., Srinivasan, R., Sánchez-Pérez, J.M., 2017. Assessment of the denitrification process in alluvial wetlands at floodplain scale using the SWAT model. Ecol. Eng. 103, 344–358. https://doi.org/10.1016/j.ecoleng.2016.06.098.
Syvitski, J.P.M., Cohen, S., Kettner, A.J., Brakenridge, G.R., 2014. How important and different are tropical rivers? - an overview. Geomorphology 227, 5–17. https://doi.org/10.1016/j.geomorph.2014.02.029.
Szabó, L., Deák, B., Bíró, T., Dyke, G.J., Szabó, S., 2020. NDVI as a proxy for estimating sedimentation and vegetation spread in artificial lakes-monitoring of spatial and temporal changes by using satellite images overarching three decades. Remote Sens. (Basel) 12 (9). https://doi.org/10.3390/RS12091468.
Tank, J.L., Rosi-Marshall, E.J., Baker, M.A., Hall, R.O., 2008. Are rivers just big streams? A pulse method to quantify nitrogen demand in a large river. Ecology 89 (10), 2935–2945. https://doi.org/10.1890/07-1315.1.
Tatariw, C., Chapman, E.L., Sponseller, R.A., Mortazavi, B., Edmonds, J.W., 2013. Denitrification in a large river: consideration of geomorphic controls on microbial activity and community structure. Ecology 94 (10), 2249–2262. https://doi.org/10.1890/12-1765.1.
Team, R.C., 2021. R: A Language and Environment for Statistical Computing (4.1.2). R Foundation for Statistical Computing. https://www.r-project.org/.
Tiedje, J.M., Sexstone, A.J., Myrold, D.D., Robinson, J.A., 1982. Denitrification: ecological niches, competition and survival. Antonie Van Leeuwenhoek 48 (6), 569–583. https://doi.org/10.1007/BF00399542.
Tuttle, A.K., McMillan, S.K., Gardner, A., Jennings, G.D., 2014. Channel complexity and nitrate concentrations drive denitrification rates in urban restored and unrestored streams. Ecol. Eng. 73, 770–777. https://doi.org/10.1016/j.ecoleng.2014.09.066.
Ullah, S., Faulkner, S.P., 2006. Denitrification potential of different land-use types in an agricultural watershed, lower Mississippi valley. Ecol. Eng. 28 (2), 131–140. https://doi.org/10.1016/j.ecoleng.2006.05.007.
van Wijk, D., Teurlincx, S., Brederveld, R.J., de Klein, J.J.M., Janssen, A.B.G., Kramer, L., van Gerven, L.P.A., Kroeze, C., Mooij, W.M., 2022. Smart Nutrient Retention Networks: a novel approach for nutrient conservation through water quality management. Inland Waters 12 (1), 138–153. https://doi.org/10.1080/20442041.2020.1870852.
Welsh, M.K., McMillan, S.K., Vidon, P.G., 2017. Denitrification along the stream-riparian continuum in restored and unrestored agricultural streams. J. Environ. Qual. 46 (5), 1010–1019. https://doi.org/10.2134/jeq2017.01.0006.
Xiong, Z., Li, S., Yao, L., Liu, G., Zhang, Q., Liu, W., 2015. Topography and land use effects on spatial variability of soil denitrification and related soil properties in riparian wetlands. Ecol. Eng. 83, 437–443. https://doi.org/10.1016/J.ECOLENG.2015.04.094.
Xiong, Z., Guo, L., Zhang, Q., Liu, G., Liu, W., 2017. Edaphic conditions regulate denitrification directly and indirectly by altering denitrifier abundance in wetlands along the Han River, China. Environmental Science and Technology 51 (10), 5483–5491. https://doi.org/10.1021/acs.est.6b06521.
Yang, Y., Dou, Y., Liu, D., An, S., 2017. Spatial pattern and heterogeneity of soil moisture along a transect in a small catchment on the Loess Plateau. J. Hydrol. 550, 466–477. https://doi.org/10.1016/J.JHYDROL.2017.05.026.
Yao, X., Zhang, L., Zhang, Y., Xu, H., Jiang, X., 2016. Denitrification occurring on suspended sediment in a large, shallow, subtropical lake (Poyang Lake, China). Environ. Pollut. 219, 501–511. https://doi.org/10.1016/j.envpol.2016.05.073.
Yi, L., Sun, Y., Ouyang, X., Yin, S., 2022. Identifying the impacts of climate change and human activities on vegetation cover changes: a case study of the Yangtze River Basin, China. Int. J. Environ. Res. Public Health 19 (10), 6239. https://doi.org/10.3390/ijerph19106239.
Yuan, L.H., Jiang, W.G., Shen, W.M., Liu, Y.H., Wang, W.J., Tao, L.L., Zheng, H., Liu, X. F., 2013. The spatio-temporal variations of vegetation cover in the Yellow River Basin from 2000 to 2010. ShengtaiXuebao/ActaEcologicaSinica 33 (24), 7798–7806. https://doi.org/10.5846/stxb201305281212.
Zucco, G., Brocca, L., Moramarco, T., Morbidelli, R., 2014. Influence of land use on soil moisture spatial–temporal variability and monitoring. J. Hydrol. 516, 193–199. https://doi.org/10.1016/J.JHYDROL.2014.01.043.
Zuur, A.F., Ieno, E.N., Smith, G.M., 2007. In: Gail, W.W.M., Krickeberg, K., Samet, J.M., Tsiatis, A. (Eds.), Analysing Ecological Data. Springer, Springer New York. https://doi.org/10.1007/978-0-387-45972-1.
Zuur, A.F., Ieno, E.N., Walker, N.J., Saveliev, A.A., G. M. S., 2009. Mixed effects models and extensions in ecology with R. In: Gail, W.W.M., Krickeberg, K., Samet, J.M., Tsiatis, A. (Eds.), Statistics for Biology and Health. Springer Science and Business Media. https://doi.org/10.4324/9780429201271-2.